Nickel L_{III} fluorescence and satellite transition probabilities determined with an alternative methodology for soft-x-ray emission spectrometry

M. Müller,[1] B. Beckhoff,[1] R. Fliegauf,[1] and B. Kanngießer[2]
[1]*Physikalisch-Technische Bundesanstalt, Abbestraße 2-12, 10587 Berlin, Germany*
[2]*Technische Universität Berlin, Hardenbergstraße 36, 10623 Berlin, Germany*
(Received 22 December 2008; published 5 March 2009)

An accurate determination of the nickel L_{III} x-ray transition probabilities was performed employing a wavelength-dispersive spectrometer (WDS) at the plane grating monochromator beamline for undulator radiation of the Physikalisch-Technische Bundesanstalt, Germany's national metrology institute, at the electron storage ring BESSY II. An absolute calibration method developed for this spectrometer improves the reliability of the determination significantly because the calibration method does not require measurements of reference samples and provides a traceable uncertainty budget. The device was calibrated with respect to both its absolute detection efficiency and its response behavior. Therefore, a method to obtain the detection efficiency of a WDS in comparison to an absolutely calibrated energy-dispersive detector was successfully applied. In addition, response functions were developed and experimentally validated. The present results for the Ni L_{III} transition probabilities differ clearly from theoretical calculations and tabulated data found in the literature. Perspectives of a quantitative study of the interactions causing the satellite transitions are outlined and discussed in view of shake-off and Coster-Kronig processes.

DOI: 10.1103/PhysRevA.79.032503 PACS number(s): 32.70.Fw, 78.70.En, 06.20.Jr, 07.85.Nc

I. INTRODUCTION

The available databases (e.g., [1–5]) providing atomic fundamental parameters (FPs) such as transition probabilities, fluorescence yields, and Coster-Kronig coefficients related to the L fluorescence of transition metals (TMs) are rather inconsistent, incomplete, and not very accurate. The main reasons are that theoretical calculations and extrapolations were predominantly used and that experimental data, if available, are often poorly documented, in particular with respect to the uncertainty budged of the experiments. In addition, only few new data have been determined in the last 30 years by state of the art theoretical or experimental methods. For example, a recently (2007) published database [1] refers to data tables from 1974 [6] and estimated uncertainties from 1978 [5]. In general, merely estimated uncertainties are available and often these uncertainties were deduced by the comparison of different databases or sets of experimental or theoretical values in compilations (e.g., [7,8]). The relative uncertainties of the FP related to the L fluorescence of the TM are assumed to be rather large (up to 40% [1]).

Nevertheless, the databases provide the best data available and except for the L fluorescence of TM and the K fluorescence of light elements, they have proven to be both reliable and very useful especially for x-ray fluorescence (XRF) analysis. The XRF method gains steadily increasing importance among nondestructive analytical methods aiming at various fields of basic research and industrial applications (i.e., process control and quality management). A thorough overview about the various applications of quantitative XRF was recently published by West *et al.* [9]. In addition, XRF employing soft x rays (below about 2 keV) has a high potential for many new materials applications due to the high dynamics of the fluorescence production and absorption of soft x rays in nanometer-scaled structures, e.g., analysis of buried nanolayers and interfaces [10,11]. In particular, grazing incident XRF gains higher deep profiling dynamics due to the increased usable incident angle range for soft x rays.

In situations where not enough adequate standards are available, i.e., when sample and standard matrices differ significantly, the most successful and commonly applied XRF quantitation method is the fundamental parameter method [12–16]. The FP method is based on the calculation of the number of fluorescence photons emitted from a sample as a function of both the sample properties (elemental composition and concentrations, thickness, layer structure, etc.) and the experimental parameters such as the beam geometry, the detector efficiency, the solid angle of detection, and the spectral characteristics and radiant power of the exciting radiation. Hence, this method uses FP to calculate quantitatively the excitation and relaxation processes within a sample of interest. In general, the determination of the instrumental parameters of the XRF setup is mainly based on measurements of reference samples. However, this method is accurate only if the reference samples are similar (rather: elements and their concentrations) to the "unknown" samples to be analyzed.

A quantitation method based on the FP method is the reference-free XRF [17–20], which is employing absolutely calibrated instrumentation. Its main advantage is to directly compare measured XRF spectra with computed fluorescence radiation intensities instead of employing any precalibration relationships derived from measurements of a set of appropriate reference samples. Anyway, both methods rely on tabulated FP and therewith on the uncertainties of the FP involved in the analysis. Hence, the lack of reliable FP values related to the L fluorescence of TM and K fluorescence of light elements strongly affects the reliability of XRF in the soft-x-ray range. This is the main motivation of the present work, the aim of which is the development of reliable experimental methods for the determination of FP in the soft-x-ray range within small and traceable uncertainties.

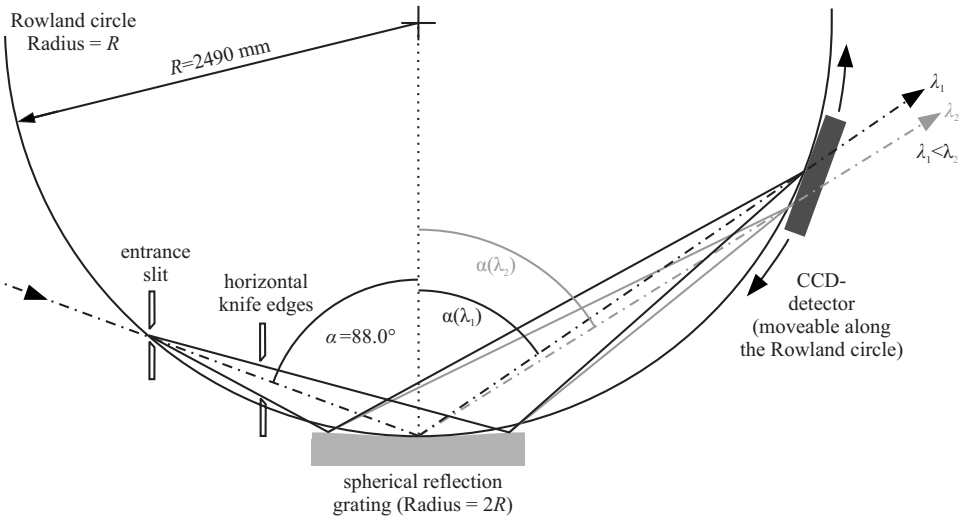

FIG. 1. Sketch of the spectrometer beam geometry. The two horizontal knife edges define a fixed illuminated area on the grating, which is important for a reliable calibration.

Using absolutely calibrated instrumentation, in particular an energy-dispersive Si(Li) detector as well as well-known synchrotron radiation [21], the absolute determination of FP has proven to be an efficient method to achieve rather small relative uncertainties (i.e., 7% for resonant Raman-scattering cross sections [22]). Basically this method is somewhat complementary to the reference-free XRF method employing thin free-standing single element foils of very high purity and known compositions as samples. FPs such as Coster-Kronig coefficients, transition probabilities, and subshell fluorescence yields associated with the soft-x-ray range cannot be well determined employing a Si(Li) detector due to its rather moderate energy resolution.[1] A high-resolution detection system is necessary to obtain many of these fundamental parameters in a reliable manner.

High-resolution x-ray emission spectroscopy has been continuously further developed over the last two decades in view of the increasing availability of synchrotron radiation. Due to the high photon flux, provided by synchrotron-radiation facilities in the soft-x-ray range, high-resolution wavelength-dispersive grating spectrometers have proven to be powerful tools for the study of soft-x-ray emission processes (see [23,24] for example). Therefore, a wavelength-dispersive spectrometer (WDS) was built to enable access to specific FP that cannot be easily obtained when using a Si(Li) detector. First results for the chemical speciation of Ti compounds obtained by the spectrometer were recently published [25]. In order to achieve small uncertainties of the FP determination employing the WDS, the absolute detection efficiency and the response behavior of the WDS have to be known as accurately as in the case of a Si(Li) detector [26].

In particular, an exact description of the response behavior is crucial for an accurate determination of the count rates of lower intensity fluorescence or satellite lines adjacent to intensive diagram lines. Therefore, priority was given to a spectrometer design that provides high stability of both the detection efficiency and the response behavior.

[1]The typical energy resolution of a Si(Li) detector is about 100 eV for the Ni $L\alpha$ fluorescence line at 851.5 eV.

II. SPECTROMETER SETUP

For the present WDS spectrometer, a concept based on the Rowland circle geometry in combination with a two-dimensional position sensitive detector was chosen. This allows for a compact and efficient design [27] and, in addition, fulfills the conditions for high stability in the best manner. The WDS consists of an entrance slit, a spherical reflection grating,[2] and a charge coupled device (CCD) detector.[3] All three elements are arranged on a Rowland circle (radius 2490 mm) and the CCD detector is movable along this circle (see Fig. 1).

An angle of incidence of 88° was chosen to ensure a good reflectivity of the Au coated grating for photon energies up to the one of Si $K\alpha$ fluorescence radiation. The design of the WDS provides very good mechanical stability,[4] high resolving power (ranging from 350 at Si $K\alpha$ energy up to 1700 at N $K\alpha$ energy for a 10 μm entrance slit width), and good detection efficiency (1.57×10^{-7} A W^{-1} sr for Ni $L\alpha$ radiation).[5]

In order to adjust the width of the entrance slit to the respective experimental requirements (resolving power vs solid angle of detection), it can be chosen between 10 and 500 μm. As detector, a thinned backside-illuminated CCD detector was chosen. This type of detector has several advantages for the detection of the dispersed radiation. It provides good linearity, detection efficiency in the soft-x-ray range [28], as well as a high spatial resolution so that an exit slit can be omitted. The most important advantage of this type of detector is the long-time stability of its detection efficiency, which is indispensable for the absolute calibration of the WDS instrument.

An additional element of the spectrometer consisting of a vertical slit and two horizontal knife edges is placed between

[2]Grating: laminar groove profile, 1200 l/mm groove density, and 4980 mm radius of curvature.

[3]CCD detector: 1024×1024 pixels, 13.5×13.5 μm^2 pixel size.

[4]E.g., a repetitious accuracy of the CCD detector position better than 1 μm.

[5]The given value is the effective spectral responsivity. See Sec. IV for details.

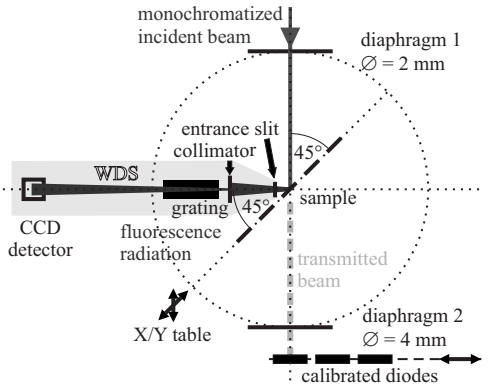

FIG. 2. Top view of the experimental XRF arrangement employing the WDS for fluorescence detection.

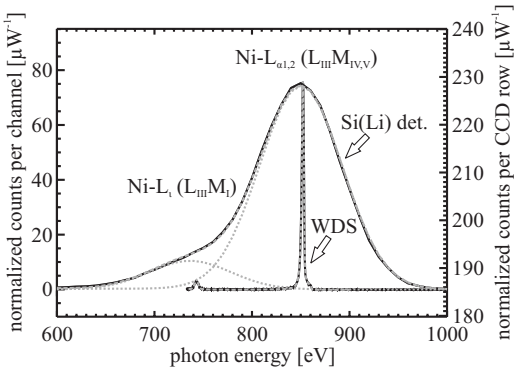

FIG. 3. Emission spectra of a thin nickel foil (black solid lines) recorded employing a calibrated Si(Li) detector and the WDS. By comparison of these spectra the detection efficiency of the WDS could be derived. The sample was excited by monochromatic radiation of 860.9 eV photon energy. The gray dashed lines are modeled curves fitted to the spectra for deconvolution purposes.

the entrance slit and the grating to function as an aperture. The width of the vertical slit is fixed at 1.0 mm and ensures that the CCD detector will not be illuminated outside its active area in the horizontal direction, i.e., in the nondispersive direction. The two horizontal knife edges are adjustable and are restricting the illuminated area of the grating in the dispersive direction. They reduce the aberration and define the acceptance angle in the plane of dispersion. Both pairs of knife edges, the vertical slit and the entrance slit, define the solid angle of detection of the WDS. A well-defined solid angle of detection is important for both the absolute measurements employing the WDS and the determination of its detection efficiency and of its response behavior.

III. EXPERIMENTAL ARRANGEMENT

Monochromatized undulator radiation, provided by the plane grating monochromator beamline of Physikalisch-Technische Bundesanstalt (PTB) at BESSY II [21,29] was employed in the current study. Figure 2 shows a sketch of the experimental arrangement. The incident beam hits the sample center at an angle of 45° in the middle of the UHV chamber employed. Emitted fluorescence or scattered radiation is detected by the WDS at an observation angle of 45°. For energy-dispersive XRF measurements the WDS can be replaced by a calibrated Si(Li) detector in combination with a calibrated aperture placed in front of the active detector area at a well-known distance from the sample center. The replacement of the detection system does not change any parameter of the setup, hence all experimental parameters for comparative measurements are exactly the same when additionally controlling the incident radiation energy and flux. The incident radiant power can be determined absolutely using a calibrated photodiode positioned behind the exit diaphragm 2. In the same arrangement, the absorption correction factors of thin samples can be experimentally determined by means of transmission measurements at both the energy of the incident radiation and the energy of the fluorescence line of interest.

IV. DETECTION EFFICIENCY AND SOLID ANGLE

The concept for the determination of the absolute WDS detection efficiency is based on the comparison of wavelength-dispersive (WD) XRF and energy-dispersive (ED) XRF measurements of the same sample under identical experimental conditions. The Si(Li) detector, employed for the XRF measurements, was calibrated absolutely with respect to both its efficiency and its response behavior [26,30]. In addition, the solid angle of detection was defined by the calibrated aperture in front of the Si(Li) detector. Therewith the number of fluorescence photons per second emitted in the solid angle could be determined absolutely. The absolute number of incident photons, which excited the sample during both the WD XRF and ED XRF measurements, was monitored by a calibrated photodiode [31].

Therewith, the product of the solid angle of detection and the detection efficiency of the WDS can be obtained for selected photon energies (e.g., of fluorescence lines of interest) in comparison to absolute energy-dispersive XRF measurements. The complex WDS apertures (entrance slit, vertical slit, and horizontal knife edges) define a fixed solid angle, but the absolute value of this solid angle is not measurable with a sufficiently small uncertainty as it is the case for the measurements employing the Si(Li) detector. Therefore, only the product of the solid angle and the detection efficiency of the WDS can be determined.

To determine the WDS detection efficiency for the nickel L-fluorescence lines, a thin free-standing Ni foil having a thickness of 0.5 μm was chosen. The energy of the exciting radiation provided by the beamline was adjusted to solely excite the L_{III} absorption edge of Ni. Therewith, only the $L\alpha$ and $L\iota$ fluorescence lines (related to $L_{III}M_{IV,V}$ and $L_{III}M_{I}$ transitions) were emitted by the sample. These two fluorescence lines could still be separated sufficiently by the Si(Li) detector (see Fig. 3). The count rates of both L_{III} related emission lines from the WDS spectrum and the Si(Li) spectrum were derived using similar deconvolution routines by employing experimentally derived response functions. The determination of the WDS response functions is described in Sec. V. The example of the Si(Li) spectra shows the advantage of employing experimentally deduced response functions, which ensure a precise determination of the $L\alpha$ and $L\iota$ count rates even when they are only partially separated.

The present calibration for the Ni $L\alpha$ photon energy results in a ratio of 0.225 between the detected count rates of the two detection systems for a WDS entrance slit width of 21.3 μm. The detection efficiency of the Si(Li) detector is 65.7% for the photon energy of the Ni $L\alpha$ radiation.

The measured signal of the CCD detector is linearly dependent on the incident radiant power because the detector is measuring the charge accumulated during the exposure time. In contrast, the signal of the Si(Li) detector is linearly dependent on the incident photon flux due to the counting of the charge pulses during the exposure time. Due to this different measurement principle of the CCD detector with respect to the Si(Li) detector the spectral responsivity is a more adequate measure for the WDS than the detection efficiency. In particular, the spectral responsivity is taking the additional proportionality of the CCD signal to the photon energy into account. The spectral responsivity is defined as the ratio between the measured current and the incident radiant power. An equivalent definition is given by the ratio of the measured number of electrons per second to the incident photon flux. Because the solid angle of the WDS could not be determined, its spectral responsivity could be derived with respect to the unit solid angle only. The spectral responsivity given with respect to the unit solid angle will be denoted as effective spectral responsivity in the following.

A value of 1.84×10^{-4} A W^{-1} for the WDS spectral responsivity for Ni $L\alpha$ radiation has been determined with respect to the solid angle of the Si(Li) detector. Normalizing this value to the unit solid angle results in a value of 9.20×10^{-8} A W^{-1} sr for the effective spectral responsivity of the WDS. Its relative uncertainty is deduced from the comparison measurements employing the WDS and the Si(Li) detector. The contributions to these relative uncertainties are the relative uncertainty of the absolute number of emitted photons determined employing the Si(Li) detector (3.3%), the Lα count rate derived from the WDS spectrum (2.5%),[6] and the Si(Li)'s solid angle of detection (0.7%). Hence, the relative uncertainty of the absolute value of the WDS detection efficiency (at Ni $L\alpha$ photon energy) sums up to a value of 4.2%.

The presented method provides only the exact spectral responsivity for photon energies of fluorescence lines, which can be resolved sufficiently by the Si(Li) detector. In the case of the CCD detector position optimized for the detection of the Ni L x-ray emission, this means the Ni $L\alpha$ and $L\iota$ lines only. Hence, a calculated dependency was used to extrapolate the relative change of the spectral responsivity over the range of all detectable photon energies for a certain CCD detector position. This dependency was calculated based on the measured reflectivity of the grating and the absorption of incident photons by a layer of incomplete charge collection at the top layer of the CCD detector. The thickness of this layer of incomplete charge collection is (63 ± 6) nm and was derived from data provided by the manufacturer of the detector. The absolute values of the calculated spectral responsivity were normalized to the absolutely determined value for the photon energy of Ni $L\alpha$. A value of the spectral responsivity for the photon energy of the Ni $L\iota$ fluorescence line was not determined absolutely, because the strong overlap of the $L\iota$ line and the intense $L\alpha$ line in the Si(Li) spectrum significantly affects the accuracy of the $L\iota$ count rate determination.

V. RESPONSE BEHAVIOR

In order to determine the response behavior of the WDS, the system was illuminated directly with monochromatized undulator radiation. Therefore the UHV chamber was rotated by 90°, allowing for a direct illumination of the WDS (0° geometry). In addition, a polycapillary optic was placed in the path of the beam 80.0 cm in front of the plane grating monochromator (PGM) beamline focus plane in order to fan out the beam. The measurements were performed during single bunch operation of the electron-storage ring BESSY II when the stored electron current was reduced by about 1 order of magnitude[7] because this prevents damages of both the polycapillary and the CCD detector.

The polycapillary was aligned first, ensuring an optimal transmittance, and then slightly misaligned to produce a wide fan-shaped beam. Therewith, the incident angle of the radiation could be chosen by aligning the vertical position of the WDS. Due to the large distance between the WDS entrance slit and the polycapillary, the divergence of the beam, which is passing through the entrance slit of the WDS, is still rather small (about 1 mrad). This nearly parallel beam illuminates a small part of the grating only and due to the small divergence the angular range of incidence is small as well. Therewith nearly no focusing took place when the incident beam was reflected at the grating. The diffraction of the incident radiation is not influenced by the effect of partial illumination, though. As long as the slit is fully illuminated the number of coherently illuminated grooves of the grating is constant, because the coherent illumination is caused solely by diffraction at the entrance slit. The coherence of the monochromatized undulator radiation is rather low and is drastically reduced by the multiple external total reflection within the polycapillary.

The images recorded by the CCD detector result in spectra showing a rather broad peak (Fig. 4). These spectra represent the spatial distribution of the radiation on the active surface of the CCD detector in the plane of dispersion of the grating. In order to determine realistic response functions it is necessary to measure the imaging characteristics as in the WD XRF measurements when the spectrometer is fully illuminated. Therefore, the angle of incidence in respect to the grating was scanned by changing the vertical position of the WDS and recording a spectrum for each angle. The maximum and the minimum angles are defined by the two horizontal knife edges which were adjusted previously in the XRF geometry.

[6]The uncertainty of the $L\alpha$ count rate derived from the WDS spectrum is deduced in the appendix.

[7]10–20 mA storage ring current instead of 200–290 mA in usual hybrid mode (mixture of multibunch and single bunch) of BESSY II.

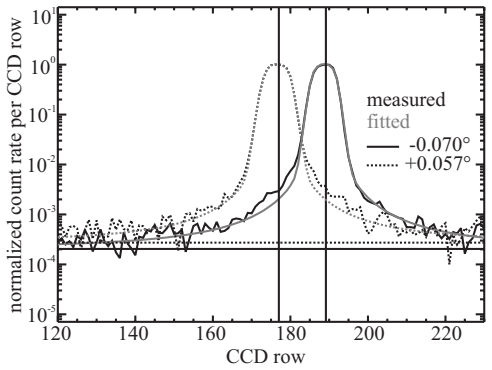

FIG. 4. Spatial distributions of the radiation incident on the CCD detector surface for two different angles of incidence with respect to the grating. The setup for these measurements was the 0° geometry and the photon energy of the monochromatized incident radiation was 771.6 eV. The first step to derive the WDS response functions is the determination of the center positions and widths by fitting modeled distributions.

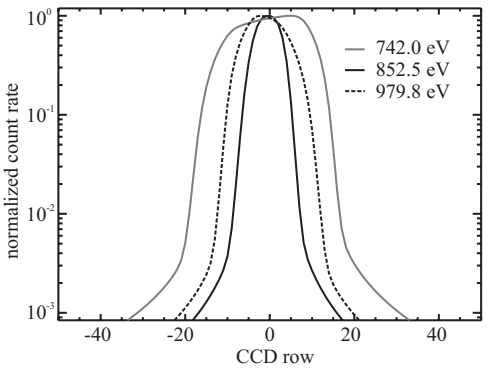

FIG. 5. Plots of the determined response function for three photon energies. The respective center positions were set to zero for the sake of a better comparability. Black solid line corresponds to an energy close to the one of Ni Lα for which the focus position of the CCD was also aiming.

To obtain the response functions of the WDS for the XRF geometry the recorded spectra have to be added in a way that the full illumination is simulated. Therefore, the angular distribution of the fluorescence radiation source spot profile in front of the entrance slit of the WDS in XRF geometry has to be simulated in an appropriate manner. Due to the nearly isotropic angular distribution of fluorescence radiation, the angular distribution of the source spot can be derived by geometric calculations from the intensity profile of the beamline in the focal plane (sample position). The beam profile at this position was measured employing another CCD detector. Due to the high photon flux provided by the undulator beamline, these measurements had to be performed during a PTB special user shift at BESSY II employing drastically reduced stored electron beam currents of about 100 μA. In this special user shift the photon flux was reduced by 3 orders of magnitude without affecting the spectral purity and the spatial distribution of the beam. The determined beam profile in the focal plane was found to have a Gaussian shape with a vertically full width at half maximum (FWHM) of 77.2 μm.

As mentioned before, the spectra of the angular scan have to be added according to the angular distribution of the source spot in order to construct the response function for a full illumination of the WDS. For practical reasons the spectra were parameterized as a function of the angle of incidence. The spatial distribution of the radiation reflected at the grating is affected by four different effects. The first one is the width of the entrance slit which can be described by a rectangularly shaped box in the spectra. The second effect is a Gaussian-shaped broadening due to the imaging characteristics of the spherical grating caused by the divergence of the incident beam. The third effect is the limited spatial resolution of the CCD detector [32] which also results in a Gaussian broadening. Both of these broadening effects cannot be distinguished from each other, but can be described satisfactorily by one combined Gaussian broadening. The fourth effect is caused by diffuse scattering on the grating and is visible as a small and very broad tailing on both sides of the measured spatial distribution (see Fig. 4). Due to the good quality of the grating the intensity of the diffuse scattered radiation is about 3 orders less than the intensity of the diffracted radiation. In addition, a minor contribution is possibly caused by the diffraction of the incident radiation at the knife edges. The overall effect including the spatial distribution of the diffraction could be well described by the equation for Fraunhofer diffraction at a slit [33].

A good approximation of the theoretical spatial distribution of the 0° geometry spectra was derived by convoluting the three functions that describe the four effects discussed above. Afterwards this theoretical spatial distribution was fitted to all the measured spectra (gray curves in Fig. 4) using a gradient-expansion algorithm to compute a nonlinear least-squares fit. The fitted parameters of interest are the center position, the width of the entrance slit, the width of the Gaussian, and a calculated contribution of the distribution caused by diffraction at the knife edges.

As the response behavior depends on the photon energy of the incident radiation, angular scans for 14 different excitation energies were performed in the 0° geometry. In order to derive the response function for every photon energy of interest, the fitted parameters of the theoretical spatial distribution for these 14 energies were parameterized with respect to the photon energy of the incident radiation. Therewith the response function of the WDS can be calculated for any photon energy at a given CCD detector position and for a given width of the entrance slit.

The quality of the resulting response functions depends on the photon energy due to the different influence of the calculated angular distribution of the source spot, caused by the energy dependent focusing. The response functions are nearly independent of the angular distribution in the case of optimal focusing. On the other hand, the broadening of the response functions for a weak focusing depends rather strongly on the angular distribution of the incident radiation. Due to this dependence the accuracy of the determined response functions is best in the region of the focus energy and decreases with decreasing resolving power.

The resulting response functions for some photon energies are plotted in Fig. 5. The CCD detector was placed at the same position as for the Ni measurements in the XRF geom-

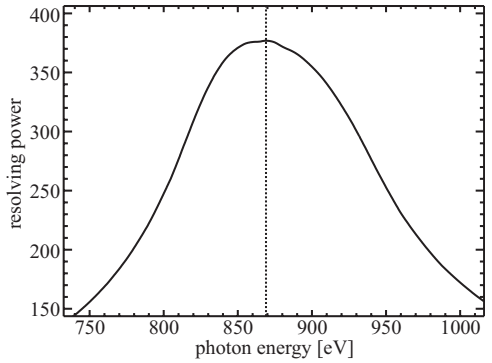

FIG. 6. The resolving power of the WDS (21.3 μm entrance slit width) derived from the response functions in the detectable energy range when the CCD detector is placed near the focus position for $L\alpha$ radiation energy.

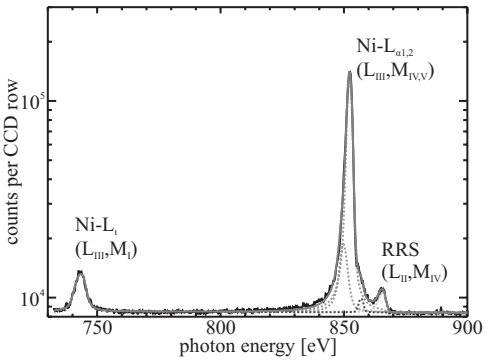

FIG. 7. X-ray emission spectrum (black) of a nominal 0.5 μm thick Ni foil excited by 867 eV photons just above the L_{III} edge (853 eV). The exposure time was 600 s. The fitted theoretical spectral distribution (gray solid line) convoluted by experimentally determined response functions is indicated for comparison.

etry. This detector position was determined to be the focus position for Ni $L\alpha$ (848.7 eV [34] or 851.5 eV [35]) fluorescence radiation.

The resolving power of the WDS was derived from the computed response functions, see Fig. 6. The adjusted detector position corresponds to the focus position for radiation of a photon energy of 869.0 eV. This focus energy matches the intended photon energy of Ni Lα fluorescence radiation quite well. The achieved maximum resolving power $E/\Delta E$ is 377 and agrees well with the theoretical maximum of 400 for an entrance slit width of 21.3 μm [36]. The resolving power was sufficient to determine the fundamental parameters of the L fluorescence radiation of Ni.

The presented method only provides an approximation of the real response functions of the WDS. However, this approximation is more adequate and more reliable than any approximation by simple Gaussian-shaped functions as will be demonstrated in Sec. VI. The response functions derived from experimental data allow for an accurate discrimination of instrumental contributions in the recorded spectra.

VI. DATA EVALUATION AND RESULTS

Transition probabilities for the hole transitions from the L_{III} shell of Ni were chosen for a first determination of fundamental parameters employing the spectrometer. Figure 7 shows the recorded spectrum of a nominal 0.5 μm thick Ni foil in a logarithmic scale, excited with monochromatic radiation of 867.0 eV photon energy. Due to this excitation below the L_{II} absorption edge at 870 eV, only the $L\alpha_{1,2}$ ($L_{\mathrm{III}}M_{\mathrm{IV,V}}$) and $L\iota$ ($L_{\mathrm{III}}M_{\mathrm{I}}$) fluorescence lines are visible in the spectrum.

The fitting of the spectral distribution was performed employing the experimentally determined response functions. The spectral distribution of the Ni fluorescence lines was described by Lorentzian functions, each of which having three free parameters (position, width, and height). This spectral distribution was modified by self-absorption effects employing experimentally determined absorption correction factors [37,22] and then multiplied with the energy-dependent detection efficiency of the WDS. In the next step this modeled distribution was convoluted with the WDS response functions. For the determination of the free parameters aiming at the best agreement to the measured spectrum a gradient-expansion algorithm to compute a nonlinear least-squares-fit was employed. The employment of the experimental response functions for the deconvolution allows for an accurate discrimination of instrumental and sample-related contributions.

The deconvolution provides a set of characteristic parameters allowing for the conversion of the spectral distribution into the count rates of both fluorescence lines without any need for self-absorption modifications or detection efficiency inclusions. Hence, the obtained count rates of the $L\alpha$ line and the $L\iota$ line are here the number N of photons per second associated with both transitions. The transition probabilities g for the Ni $L_{\mathrm{III}}M_{\mathrm{IV,V}}$ and $L_{\mathrm{III}}M_{\mathrm{I}}$ transitions arise from

$$g_j = \frac{N_j}{N_j + N_i}, \quad (j = L_\alpha, i = L\iota \text{ or } j = L\iota, i = L_\alpha). \qquad (1)$$

The determination of L_{III} transition probabilities is not strongly affected by the chosen model for the response functions because the two fluorescence lines are well separated and only slightly overlapping with other spectral features. On the other hand, the Ni emission spectrum becomes more complex with increasing incident photon energy. First, a spectral feature of resonant Raman scattering[8] (RRS) becomes visible in the spectra with increasing energy (see Fig. 7). The energetic position and intensity of the RRS feature scale with the incident photon energy. For photon energies below 870 eV the RRS feature overlaps with the $L\alpha_{1,2}$ fluorescence lines as in the case discussed before. This overlap affects the accuracy of the area determination for both the $L\alpha_{1,2}$ transitions and the RRS transition. In this situation the use of experimentally derived response functions is quite helpful to still ensure a good accuracy in spite of this overlap.

[8]Also often called resonant inelastic x-ray scattering (RIXS).

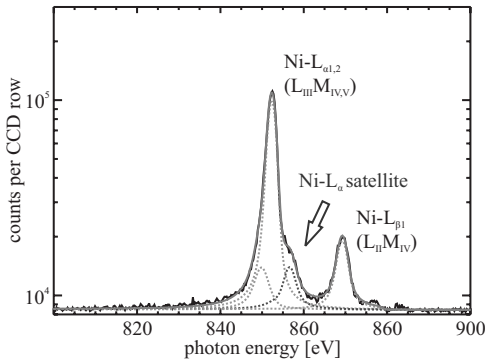

FIG. 8. X-ray emission spectrum (black) of a nominal 0.5 μm thick Ni foil excited by 879 eV photons just above the L_{II} edge (871 eV). The exposure time was 600 s. The fitted theoretical spectral distribution convoluted by experimentally determined response functions (gray solid line) is indicated for comparison.

The difficulties originating from overlapping spectral distributions increase with increasing incident photon energy above the Ni L_{II} absorption edge. Figure 8 shows a part of the spectrum recorded for an incident photon energy of 879 eV. Besides the $L\beta_1$ ($L_{II}M_{IV}$) transition a shoulder at the high energy side of the $L\alpha$ transition is visible in the spectrum. This shoulder probably belongs to an $L\alpha$ satellite transition, which is usually ascribed to a spectator vacancy created by shake off and preceding Coster-Kronig transition [38–40]. The details about the involved excitation and relaxation processes and their importance are still in discussion. The satellite transition is separated from the $L\alpha$ line by only a few eV and, in addition, is much less intense than the diagram line. Due to the employment of the experimentally determined response functions, deconvolution of the shown spectrum is still reliable and accurate.

A detailed evaluation of the uncertainties can be found in the Appendix. The relative uncertainties of the determined transition probabilities are 0.55% and 5.6% for the Ni Lα and Ni $L\iota$ transitions, respectively. The standard variation Δg_j of the determined transition probabilities is 0.5%.

The resulting transition probabilities for the nickel $L\alpha$, $L\alpha_{satellite}$, and $L\iota$ lines are listed in Table I. All transition probabilities were determined employing the deconvolution procedure described above, which is taking into account both the self-absorption within the sample and the spectral responsivity of the WDS. A rather good agreement of the values, derived from the two shown spectra, could be achieved by considering the $L\alpha$ and $L\alpha_{satellite}$ lines as one line. The $L\iota$ transition probabilities, determined by excitation below and above the L_{II} edge, barely agree within their respective uncertainties. This is probably due to a rearrangement of the $3d$ shell caused by preceding Coster-Kronig transitions and the shake processes in the case of the excitation above the L_{II} edge. In this case the transition probability of the satellite line is 10% and therewith the probability of a preceding Coster-Kronig transition or shake process, which creates a doubly ionized atomic state, is at least 10% as well.

For the sake of comparison two values from recent databases were additionally listed in Table I. These values differ clearly from the values determined in the present work. In particular, the values of the $L\iota$ transition probabilities are significantly smaller in the references (up to 25% relative difference).

VII. DISCUSSION

An evaluation of the experimentally determined WDS response functions was done by fitting modeled spectral distributions to measured WDS spectra employing the experimental and Gaussian-shaped response functions and comparing the results. A clearly visible difference between the results cannot easily be stated and the least-squares criteria show some limited differences only. The reason for the latter is the relatively high symmetry of the experimentally determined response functions resembling to a certain extent the one of a Gaussian. Here, concerning the agreement of fitted and measured spectra one may conclude that the use of experimental response functions ensures a similar quality as in the case of employing Gaussian functions, the latter, however, with additional degrees of freedom due to the independent Gaussian widths. Thus, experimental response functions have advantages when dealing with more complex spectra due to their lower total number of degrees of freedom.

To be more specific, both deconvolution methods show significant differences in the results obtained for the count rates of the respective transitions. In particular, the obtained count rates of the transitions with low intensity have rather large discrepancies. For example, the count rate of the satellite transition obtained employing the experimental response

TABLE I. Transition probabilities for the Ni $L\alpha_{1,2}$ and Ni $L\iota$ fluorescence lines. For a better comparability to the values taken from the references the determined transition probabilities of the Ni $L\alpha_{1,2}$ diagram line and the satellite line were added.

Reference	$L\alpha_{1,2}$ including satellite	$L\alpha_{1,2\ satellite}$	$L\iota$
Present work (excited at 867 eV below L_{II} edge)	0.908 ± 0.005	0.013 ± 0.005	0.092 ± 0.005
Present work (excited at 879 eV above L_{II} edge)	0.915 ± 0.006	0.100 ± 0.005	0.085 ± 0.005
Zschornack[a]/Scofield[b]	0.931		0.069
Elam *et al.*[c]/Salem *et al.*[d]	0.925		0.075

[a]Reference [1].
[b]Reference [6].
[c]Reference [34].
[d]Reference [41].

functions is 50% larger than in the case of using Gaussian functions. Another difference in the results of both methods is the behavior of the $L\alpha_2$ transition, which could be assigned more correctly to the asymmetric band structure of the $3d$ shell. A closer look at spectra recorded at different incident photon energies shows that the count rates of the $L\alpha$ transitions obtained employing the Gaussian functions are randomly distributed and only their sum is constant. The deconvolution employing the experimental response functions shows a considerably more stable determination of the count rate of each single transition, most probably due to the lower degree of freedom as a strict constraint for spectral deconvolution. In particular, this is again important for a reliable quantitation of small spectral features overlapping with intense diagram lines, as for example, the satellite line adjacent to the $L\alpha_{1,2}$ transition.

The results for the transition probabilities of the $L\alpha$ satellite line are interesting in view of shake-off and Coster-Kronig processes. Magnuson *et al.* [38] reported that a significant part of the spectator vacancies related to the $L\alpha$ satellites of Cu is created by shake-off processes during the photoionization. About 10% of the ionized Cu atoms are double-ionized by shake-off processes at excitation energies below the L_{II} edge. In the case of nickel only 1.3% of the ionized atoms seem to be doubly ionized by shake-off processes. Another difference between Cu and Ni is the higher relative intensity of the Cu $L\alpha$ satellite transitions (about 40% [38]) with respect to the Ni satellite (10%). One reason could be the increased occupation of the N shells of Cu and therewith an increased transition rate of the L_{II}-L_{III}N Coster-Kronig transitions [39]. Another reason could be a change in possible L_{II}-$L_{\mathrm{III}}M_{\mathrm{IV,V}}$ Coster-Kronig transition channels, which are not easily predictable for solid-state specimens.

VIII. CONCLUSION

The design of the presented wavelength-dispersive spectrometer allows for a reliable characterization of both the response behavior and detection efficiency. In particular, the use of experimentally determined response functions allow for an accurate discrimination of instrumental and sample-related contributions in the spectra, which significantly improves the accuracy of the spectrum deconvolution with respect to the physical processes of interest.

Rather small relative uncertainties were achieved for both the determination of the absolute WDS detection efficiency at the photon energy of Ni $L\alpha$ radiation (4.2%) and the spectra deconvolution employing the response functions (2.5%–5.0%). Due to the restriction of using fluorescence radiation at related discrete photon energies only, the detection efficiency of the full detectable energy range has to be interpolated and extrapolated beyond the energies provided by intense fluorescence lines. To improve the reliability of this extrapolation a calibration of the CCD detector will be performed employing the calibrated instrumentation of PTB.

The initial results already demonstrate that atomic fundamental parameters related to the soft-x-ray range can be determined with rather small relative uncertainties when employing the spectrometer. Once the characterization of the employed spectrometer is completed, selected fundamental parameters such as Coster-Kronig coefficients, fluorescence yields, and resonant Raman-scattering cross sections will be accessible with relative uncertainties of less than 10%.

The first quantitative values of the Ni $L\alpha$ satellite transition probability could be derived in the present work with good accuracy (uncertainty less than 0.5%). These two values suggest that the origin of the involved spectator vacancy is mainly caused by preceding Coster-Kronig transitions. A more detailed comparison of satellite transition probability, shake-off probabilities, and Coster-Kronig transition probabilities may give a clearer picture of the involved excitation and relaxation channels. Therefore, the transition probabilities of the satellite line will be determined in the near future at more excitation energies across the Ni L absorption edges.

ACKNOWLEDGMENTS

The financial support of this research activity within the frame of the ProFiT project "Quantitation in x-ray fluorescence analysis" supported by the Investitionsbank Berlin is gratefully acknowledged.

APPENDIX: UNCERTAINTY EVALUATION

To simplify the determination of the uncertainty of the obtained transition probabilities Eq. (A1) was used to approximate the determination of the transition probabilities. This equation contains the following simplifications. First of all, in the uncertainty evaluation the fluorescence lines were considered as monochromatic lines at the respective center energies only. Therewith, the ratio ε' of the detection efficiency at Ni $L\alpha$ and Ni $L\iota$ center photon energies could be defined [see Eq. (A2)]. This is a useful simplification because the absolute values of the WDS detection efficiency $\varepsilon(E)$ at the Ni $L\alpha$ and Ni $L\iota$ photon energies E are directly entering the determination of the transition probabilities, whereas only the ratio ε' of the detection efficiency at these two energies has an actual effect.

The uncertainties of the determined count rates are caused by the uncertainties of the spectra deconvolution. The accuracy of the spectra deconvolution is affected by the accuracy of the employed response functions and the absorption correction factors. The relative uncertainties of the count rates for the $L\alpha$ line and for the $L\iota$ line induced by the deconvolution of the spectra employing the experimentally determined response functions were estimated to be about 2.5% and 5.0%, respectively. The difference is caused by the response functions, which are less precise for the $L\iota$ line energy region than for the $L\alpha$ line region, as mentioned in Sec. V. The estimation of the uncertainties is based on a comparison of the fitting results of many different spectra and, in addition, on a comparison of fitting results and region of interest evaluations of spectra without a significant overlapping of different spectral features

$$g_j \approx \frac{I_j}{I_j + \varepsilon'_{ji} I_i}, \quad I_j = \varepsilon(E_j) N_j,$$

$$j = L\alpha, i = L\iota \text{ or } j = L\iota, i = L\alpha, \tag{A1}$$

$$\varepsilon'_{ji} = \frac{\varepsilon(E_j)}{\varepsilon(E_i)}. \tag{A2}$$

The relative uncertainty of the self-absorption correction factor is mainly caused by a slight disagreement between the energy scales of the WDS spectrum and the transmission measurement of the sample at the PGM beamline. The influence of this disagreement is most significant for the $L\alpha$ count rate due to the adjacent L_{III} absorption edge. It was found that the agreement of the two energy scales is better than 0.1 eV. This slight disagreement affects the accuracy of the self-absorption correction and results in a contribution of about 0.7% and 0.11% to the relative uncertainty of the derived count rates I of the $L\alpha$ and $L\iota$ lines, respectively.

The relative uncertainty of the ratio ε' of the WDS detection efficiency at the center photon energies of Ni $L\alpha$ and Ni $L\iota$ is deduced from the relative uncertainty of the derived thickness of the layer of incomplete charge collection on the top of the CCD detector as well as the relative uncertainty of the measured efficiency of the grating, which is less than 1% [42]. It is negligible with respect to the relative uncertainty of the layer thickness which was estimated to be about 10%. The influence on the ratio ε' was studied by varying the thickness of the layer of incomplete charge collection. It was found that the influence of the thickness is rather small on the ratio ε'. The relative uncertainty of the thickness causes a relative change of the ratio ε' of 1.1% only.

Equation (A3) is derived from Eq. (A2) by carrying out error propagation. Using this equation one gets 0.5% as the standard variation Δg_j for the determined transition probabilities

$$\frac{\Delta g_j}{g_j} \approx g_i \sqrt{\left(\frac{\Delta I_j}{I_j}\right)^2 + \left(\frac{\Delta I_i}{I_i}\right)^2 + \left(\frac{\Delta \varepsilon_i}{\varepsilon_i}\right)^2}. \tag{A3}$$

[1] G. Zschornack, *Handbook of X-Ray Data* (Springer, New York, 2007).
[2] W. T. Elam, B. D. Ravel, and J. R. Sieber, Radiat. Phys. Chem. **63**, 121 (2002).
[3] J. H. Scofield, Phys. Rev. A **10**, 1507 (1974).
[4] W. Bambynek, B. Crasemann, R. W. Fink, H. U. Freund, H. Mark, C. D. Swift, R. E. Price, and P. Venugopala Rao, Rev. Mod. Phys. **44**, 716 (1972).
[5] M. Krause, C. Nestor, C. Sparks, and E. Ricci, Oak Ridge National Laboratory Report No. ORNL-5399, 1978 (unpublished).
[6] J. H. Scofield, At. Data Nucl. Data Tables **14**, 121 (1974).
[7] J. L. Campbell and T. Papp, At. Data Nucl. Data Tables **77**, 1 (2001).
[8] J. L. Campbell, At. Data Nucl. Data Tables **95**, 115 (2009).
[9] M. West, A. T. Ellis, P. Kregsamer, P. J. Potts, C. Streli, C. Vanhoff, and P. Wobrauschek, J. Anal. At. Spectrom. **23**, 1409 (2008).
[10] P. Hönicke, B. Beckhoff, M. Kolbe, S. List, T. Conard, and H. Struyff, Spectrochim. Acta, Part B **63**, 1359 (2008).
[11] B. Pollakowski, B. Beckhoff, F. Reinhardt, S. Braun, and P. Gawlitza, Phys. Rev. B **77**, 235408 (2008).
[12] R. M. Rousseau, X-Ray Spectrom. **13**, 115 (1984).
[13] R. M. Rousseau, X-Ray Spectrom. **13**, 121 (1984).
[14] M. Mantler, Adv. X-Ray Anal. **36**, 27 (1992).
[15] M. Kaufmann, M. Mantler, and F. Weber, Adv. X-Ray Anal. **39**, 701 (1997).
[16] M. Mantler, J. P. Willis, G. R. Lachance, B. A. R. Vrebos, K.-E. Mauser, N. Kawahara, R. M. Rousseau, and P. N. Brouwer, in *Handbook of Practical X-Ray Fluorescence Analysis*, edited by B. Beckhoff, B. Kanngießer, N. Langhoff, R. Wedell, and H. Wolff (Springer, New York, 2006), pp. 309–410.
[17] M. Kolbe, B. Beckhoff, M. Krumrey, and G. Ulm, Spectrochim. Acta, Part B **60**, 505 (2005).
[18] B. Beckhoff, R. Fliegauf, M. Kolbe, M. Müller, J. Weser, and G. Ulm, Anal. Chem. **79**, 7873 (2007).
[19] B. Beckhoff, J. Anal. At. Spectrom. **23**, 845 (2008).
[20] A. Owens, B. Beckhoff, G. Fraser, M. Kolbe, M. Krumrey, A. Mantero, M. Mantler, A. Peacock, M.-G. Pia, D. Pullan, G. Ulm, and U. Schneider, Anal. Chem. **80**, 8398 (2008).
[21] F. Scholze, B. Beckhoff, G. Brandt, R. Fliegauf, A. Gottwald, R. Klein, B. Meyer, U. Schwarz, R. Thornagel, J. Tümmler, K. Vogel, J. Weser, and G. Ulm, Proc. SPIE **4344**, 402 (2001).
[22] M. Müller, B. Beckhoff, G. Ulm, and B. Kanngießer, Phys. Rev. A **74**, 012702 (2006).
[23] J. Nordgren and N. Wassdahl, Phys. Scr. **T31**, 103 (1990).
[24] J. Nordgren, P. Glans, and N. Wassdahl, Phys. Scr. **T34**, 100 (1991).
[25] F. Reinhardt, B. Beckhoff, H. Eba, B. Kanngießer, M. Kolbe, M. Mizusawa, M. Müller, B. Pollakowski, K. Sakurai, and G. Ulm, Anal. Chem. **81**, 1770 (2009).
[26] F. Scholze and M. Procop, X-Ray Spectrom. **30**, 69 (2001).
[27] J. Nordgren, G. Bray, S. Cramm, and R. Nyholm, Rev. Sci. Instrum. **60**, 1690 (1989).
[28] Yuelin Li, G. D. Tsakiris, and R. Sigel, Rev. Sci. Instrum. **66**, 80 (1995).
[29] F. Senf, U. Flechsig, F. Eggenstein, W. Gudat, R. Klein, H. Rabus, and G. Ulm, J. Synchrotron Radiat. **5**, 780 (1998).
[30] F. Scholze, B. Beckhoff, M. Kolbe, M. Krumrey, M. Müller, and G. Ulm, Mikrochim. Acta **155**, 275 (2006).
[31] A. Gottwald, U. Kroth, M. Krummrey, M. Richter, F. Scholze, and G. Ulm, Metrologia **43**, S125 (2006).
[32] G. Ghiringhelli, A. Piazzalunga, C. Dallera, G. Trezzi, L. Braicovich, T. Schmitt, V. N. Strocov, R. Betemps, L. Patthey, X. Wang, and M. Grioni, Rev. Sci. Instrum. **77**, 113108 (2006).
[33] M. Born and E. Wolf, *Principles of Optics*, 6th ed. (Pergamon, New York, 1980), Chap. 8.5.1.
[34] W. T. Elam, B. D. Ravel, and J. R. Sieber, Radiat. Phys. Chem. **63**, 121 (2002).
[35] J. A. Bearden, Rev. Mod. Phys. **39**, 78 (1967).
[36] W. B. Peatman, *Gratings, Mirrors and Slits: Beamline Design For Soft X-Ray Synchrotron Radiation Sources* (Gordon and Breach, New York, 1997), Chap. 4.
[37] B. Beckhoff and G. Ulm, Adv. X-Ray Anal. **44**, 349 (2001).

[38] M. Magnuson, N. Wassdahl, and J. Nordgren, Phys. Rev. B **56**, 12238 (1997).
[39] S. L. Sorensen, S. J. Schaphorst, S. B. Whitfield, B. Crasemann, and R. Carr, Phys. Rev. A **44**, 350 (1991).
[40] N. Wassdahl, J.-E. Rubensson, G. Bray, P. Glans, P. Bleckert, R. Nyholm, S. Cramm, N. Mårtensson, and J. Nordgren, Phys. Rev. Lett. **64**, 2807 (1990).
[41] S. I. Salem, S. L. Panossian, and R. A. Krause, At. Data Nucl. Data Tables **14**, 91 (1974).
[42] R. Klein, C. Laubis, R. Müller, F. Scholze, and G. Ulm, Microelectron. Eng. **83**, 707 (2006).